Trapping and tracking a local probe with a photonic force microscope

Alexander Rohrbach,[a] Christian Tischer, Dirk Neumayer, Ernst-Ludwig Florin, and Ernst H. K. Stelzer
European Molecular Biology Laboratory (EMBL), Meyerhofstrasse 1, Postfach 102209, D-69117 Heidelberg, Germany

(Received 16 June 2003; accepted 25 February 2004; published online 28 May 2004)

An improved type of scanning probe microscope system able to measure soft interactions between an optically trapped probe and local environment is presented. Such a system that traps and tracks thermally fluctuating probes to measure local interactions is called a photonic force microscope (PFM). The instrument can be used to study two-dimensional and three-dimensional surface forces, molecular binding forces, entropic and viscoelastic forces of single molecules, and small variations in particle flow, local diffusion, and viscosities. We introduce and characterize a PFM, and demonstrate its outstanding stability and very low noise. The probe's position can be measured within a precision of 0.2–0.5 nm in three dimensions at a 1 MHz sampling rate. The trapping system facilitates stable trapping of latex spheres with diameter $D=\lambda_0/2$ at laser powers as low as 0.6 mW in the focal plane. The ratio between the trapping stiffness and laser power was able to be optimized for various trapping conditions. The measured trap stiffnesses coincide well with the calculated stiffnesses obtained from electromagnetic theory. The design and the features of the novel PFM setup are discussed. The optical and thermodynamical principles as well as signal analysis are explained. Applications for three-dimensional, hard-clipping interaction potentials are shown. The technique discussed in this article and the results presented should be of great interest also to people working in the fields of classical optical tweezing, particle tracking, interferometry, surface inspection, nanotechnology, and scanning probe microscopy. © *2004 American Institute of Physics.* [DOI: 10.1063/1.1753097]

I. INTRODUCTION

Thermal fluctuations of the transducer unit are often the limiting factor for resolution and precision in most local probing systems. Typical examples are thermal vibrations of the cantilever of an atomic force microscope (AFM)[1,2] or of a small sphere captured by optical tweezers.[3,4] The fine tip of an AFM cantilever, although excellent for high-precision surface scanning, is too stiff to pick up the thermal motion of the sample. In contrast, optical trapping systems use spherical particles with diameters between 100 nm and 10 μm as transducers. These are much larger than an AFM tip, but can be trapped with stiffnesses, which are 100–1000 times softer than that of the AFM cantilever. Moreover, unlike the cantilever tip of an AFM, the trapped particle does not have any mechanical contact with the sample so their use is therefore not restricted to surface measurements.

Thermal motion provides a mechanism by which a molecule or a cell component can find the optimal interaction with its environment. The random fluctuations in position and orientation enable "trial and error" sampling of interaction states, which is necessary when passing through process cascades. Because of this optimization concept, it seems reasonable to exploit thermal fluctuations in biological or biochemical experiments to measure the interaction of organelles, proteins, or macromolecules with their environment. The thermal fluctuations of small particles are determined by their environment (mainly by its temperature and viscosity) and are altered when external forces act on the fluctuating probes. It is therefore desirable to record the three-dimensional position fluctuations of a particle as it interacts with its environment. To prevent the probe from diffusing away from the region of interest, it is advantageous to use an optical trap to apply forces that restrict the range of the diffusing particle. The three-dimensional trajectory of the particle can be tracked interferometrically. From the histogram of particle positions it is possible to deduce the interaction potential and the corresponding forces that act on the particle. These are the ideas behind a photonic force microscope (PFM) (see the schematic in Fig. 1).

Thermal fluctuations play a less important role when optical tweezers are used to move particles from one point to another[5–11] than when they were used to measure small forces such as those in single molecule experiments.[12–18] Here the precision of position and force measurements is limited by the thermal fluctuations of the probe in the trap, even when minimized with, e.g., feedback systems.[19,20] Thermal position fluctuations of a trapped probe are exploited to calibrate optical traps, e.g., in the Langevin method, where the particle fluctuates inside a volume, defined by the three-dimensional (3D) histogram of the particle's center positions. This *trapping volume* can be smaller than the optical focus volume that generates the trap. Depending on the laser power and probe diameter, these ellipsoidal trapping volumes can vary in size by more than three orders of magnitude with extents as small as $\lambda_0/30\times\lambda_0/100$ (λ_0 is the trapping wavelength in vacuum). In the PFM, fluctuations of the probe's position can be utilized in applications such as the measurement of interactions with two-dimensional (2D) and 3D sur-

[a]Electronic mail: rohrbach@embl-heidelberg.de

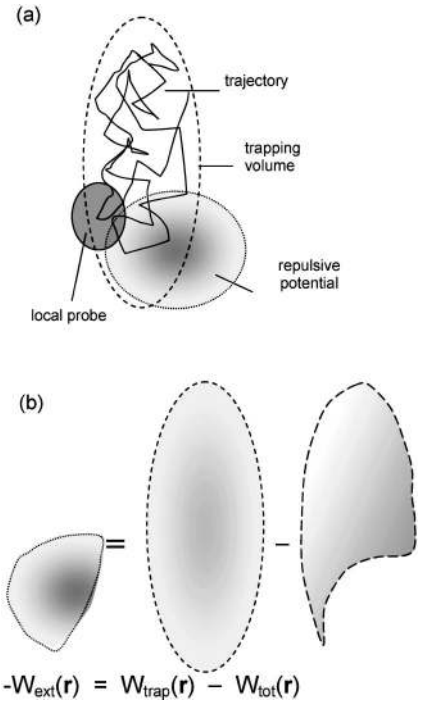

FIG. 1. Schematic of the interaction between the local probe and an external potential. (a) The trajectory of the fluctuating particle is confined by the optical trapping volume and the (repulsive) external potential. (b) The external potential $W_{ext}(\mathbf{r})$ can be recovered by the difference between the unobstructed trapping potential $W_{trap}(\mathbf{r})$ and the total potential $W_{tot}(\mathbf{r})$ in the presence of the external potential.

faces,[21–23] receptor–ligand interaction, local changes of viscosity[24] and diffusion,[25] tiny flows, or the properties of single molecule experiments.[26,27]

The main difference between the PFM and conventional optical tweezers is that the latter measure a force along a specific direction after the trap is calibrated. A PFM provides the complete 3D potential from a histogram of recorded positions. The main differences from other particle tracking systems, which also record position histograms, are that these work with video cameras (30 Hz–10 kHz), are able to measure several particles in parallel, and are limited in axial position detection. A PFM can track a single particle in three dimensions with nanometer precision at rates of 1 MHz, which enables the determination of the potential landscape with much better resolution.

The idea of scanning a trapped probe along or over a sample to image its surfaces is more than 10 years old[28] and has experienced several variations.[22,29–32] In most cases, thermal noise was regarded as a disturbance. Brownian motion of the probe was exploited for the first time to calibrate the optical trap.[29,33] However, except for a few studies[34–38] this was done only in directions perpendicular to the optical z axis, assuming that the motion of the probe along z is very small ($<\lambda/4$) and that the lateral xy signal is constant over that axial range. A typical example of this assumption is linking a probe to a surface in the xy plane.[25,39] For soft axial forces, however, the resulting z fluctuations of the probe reveal important information about coupling to the surface and must not be neglected.

The goal of this article is to explain how to set up and characterize a PFM. The literature on optical trapping systems from the last decade discusses and emphasizes the necessity of mechanical stability, laser stability, speed and precision of position detection, trapping efficiency, robustness, and flexibility for different experimental configurations. In addition, it was pointed out[40] that the differences between theoretically predicted and measured trapping forces were unsatisfactory (often more than 100% for subwavelength particles). The improvements that we have made in the PFM's stability, trapping efficiency, tracking accuracy, and speed further motivated us to write this article. We expect this to be of great interest also for people working in the field of classical optical tweezing, particle tracking, interferometry, surface inspection, nanotechnology, or scanning probe microscopy. We demonstrate how and to what extent, mechanical stability, fast precise particle tracking, and a diffraction limited optical trap push a trapping system to the physical limits. This requires low system background noise (three to four orders of magnitude smaller than the signal), probe position detection with nanometer precision at a MHz sampling rate, and trapping stiffnesses that can be varied over three orders of magnitude at low laser power. We restrict our investigations to dielectric probes with dimensions between $\lambda_0/10$ and λ_0, the range of so-called Rayleigh–Debye scatterers, which are especially interesting for single molecule experiments, probing inside biological systems, and application in nanotechnology.

The principles behind the PFM are explained in Sec. II. The PFM apparatus is presented in Sec. III where special emphasis is placed on the optics. The performance of the PFM detection system is discussed in Sec. IV, and Sec. V treats the PFM's background noise. In Sec. VI position analyses of the probe's fluctuations and the resulting trapping potentials demonstrate that the optical traps generated by our PFM are at the physical limit imposed by diffraction and polarization of the field in the focus. Experimental results of trap stiffness are compared with results from computer simulations. Imaging a plane surface by a fluctuating probe bridges to 3D thermal noise imaging, which is shown in Sec. VIII. We also describe calibration of both trap and detector by thermal fluctuations to complete the description of photonic force microscopy (Sec. VII).

II. PRINCIPLES

The principles behind the PFM are outlined in Fig. 2. An objective lens (OL) with a high numerical aperture (NA) focuses a collimated laser beam, resulting in strong intensity gradients. Scattering and optical forces occur due to the interaction of light with a particle near the focus. If the intensity gradients result in a gradient force that is stronger than the radiation pressure (the scattering force), the particle will be drawn towards the stable trapping point $\mathbf{r}_0$ where the sum of the forces is $\mathbf{F}(\mathbf{r}_0)=0$. This point $\mathbf{r}_0$ is slightly behind the point of maximum intensity in the focus because of the scattering force. Due to collisions with molecules in the surrounding fluid, the particle experiences a random thermal force $\mathbf{F}_{th}(t)$ that displaces the trapped particle from its resting position $\mathbf{r}_0$. The restoring optical force $\mathbf{F}_{opt}$ is linear with

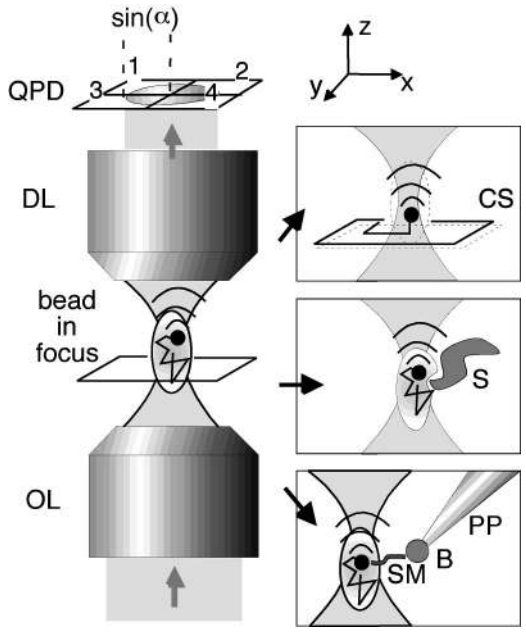

FIG. 2. Principles behind a photonic force microscope. A laser beam is tightly focused by a high NA objective lens (OL). The incident light is scattered by the local probe in the focal region and resultant optical forces generate a three-dimensional optical trap. The local probe explores the trapping volume due to Brownian motion. Light scattered by the probe and unscattered light generate an interference pattern, which is projected by a detection lens (DL) onto a quadrant photodiode (QPD) that is placed in the back focal plane (BFP) of the detection lens. The quadrants are numbered by 1–4. The detector signals generated by the fluctuating probe are analyzed to determine interaction with the local environment. Typical experiments are outlined by three boxes on the right: (a) The probe is fixed to a coverslip (CS), which is moved with the stage along a specific path to characterize the detection system. (b) A structure (S) penetrates and alters the trapping volume of the fluctuating probe, disclosing the interaction between structure and probe. (c) A single molecule (SM) is tethered between the local probe in the trap and a bead (B) attached to a micropipette (PP) to measure the visco elastic properties of the molecule.

the displacement $(\mathbf{r}-\mathbf{r}_0)$, i.e., $\mathbf{F}_{\mathrm{opt}}(\mathbf{r})=\boldsymbol{k}(\mathbf{r}-\mathbf{r}_0)$ over a range of about $\lambda_0/2$ in axial and $\lambda_0/4$ in lateral directions. The motion of a sphere with radius a experiences a friction force $\mathbf{F}_{\mathrm{fric}}(\mathbf{r},t)=\gamma(\mathbf{r})_i\mathbf{v}(\mathbf{t})$ with velocity $\mathbf{v}(\mathbf{t})$, viscous drag $\gamma(\mathbf{r})=6\pi a\,\eta(\mathbf{r})$, and spatially varying viscosity $\eta(\mathbf{r})$ of the medium surrounding the probe. The corresponding equation of motion is the Langevin equation,[41]

$$\underbrace{m\ddot{\mathbf{r}}(t)}_{\to 0}+\underbrace{[\gamma(\mathbf{r})\dot{\mathbf{r}}(t)-\mathbf{F}_{\mathrm{th}}(t)]}_{\text{microscopic scanner}}+\underbrace{\mathbf{F}_{\mathrm{opt}}(\mathbf{r})}_{\substack{\text{macroscopic}\\ \text{scanner}}}+\underbrace{\mathbf{F}_{\mathrm{ext}}(\mathbf{r},t)}_{\text{measurand}}=0. \tag{1}$$

Here m is the mass of the particle and the measurand $\mathbf{F}_{\mathrm{ext}}(\mathbf{r},t)$ is an external force that acts on the probe in the optical trap. The particle undergoes thermal position fluctuations that are mainly determined by the friction force (viscous drag) and the random force $\mathbf{F}_{\mathrm{th}}(t)$, which depends on the temperature and the viscous drag. This forms the microscopic scanning unit, whereas the optical trap specifies the volume and the location of the thermal fluctuations (macroscopic scanner).

The idea of measuring the interaction of a trapped probe with its local environment is shown schematically in Fig. 1(a). The three-dimensional trajectory of the fluctuating probe is altered in the presence of an external potential, which repels or attracts the particle or changes its temporal behavior due to variations in viscosity. According to Boltzmann statistics a potential $W(\mathbf{r})$ that acts on the probe can be obtained from its position histogram (see Sec. VI B). The difference between the pure trapping potential $W_{\mathrm{trap}}(\mathbf{r})$ measured in bulk solution and the distorted potential $W_{\mathrm{tot}}(\mathbf{r})$ yields the external interaction potential $W_{\mathrm{ext}}(\mathbf{r})$ that acts on the probe [see Fig. 1(b)].

Equation (1) describes the probe's motion, which can be monitored by the light scattered by the probe. As shown in Fig. 2, a detection lens (DL) with angular aperture $\sin(\alpha)$ collects the interference of scattered and unscattered light at the back-focal plane (BFP) of the detection lens. A quadrant photodiode (QPD) placed at the BFP or a conjugate plane records varying interference patterns $I[\mathbf{r}(t)]$ that occur due to spatiotemporal displacements $\mathbf{r}(t)$ of the probe. The resulting three-dimensional position signal $\mathbf{S}[\mathbf{r}(t)]$ is a nonlinear function of $I[\mathbf{r}(t)]$. The insets on the right of Fig. 2 illustrate three different combinations of how a probe's motion through the trapping focus is measured with the quadrant photodiode: (a) a controlled movement of the probe, attached to a coverslip (CS) is used for system characterization. (b) The diffusing probe interacts with a structure (S), which penetrates the trapping volume and alters the probe's fluctuations by changing $\gamma(\mathbf{r})$ and/or exerting an external force $\mathbf{F}_{\mathrm{ext}}(\mathbf{r},t)$ on the probe. (c) A single molecule (SM) is tethered between the local probe in the trap and a bead (B) attached to a micropipette (PP). By displacing either the trap or the pipette, the viscoelastic properties of the molecule or force $\mathbf{F}_{\mathrm{ext}}(\mathbf{r},t)$ exerted by the molecule on the probe can be measured.

III. APPARATUS

The PFM consists of mechanical, optical, and electronic components. The PFM makes use of an easily accessible microscope stand, which is illustrated in the photo in Fig. 3. Its frame and most of its mounts are made of steel and cast iron to achieve maximum mechanical and temperature stability. Special care was taken at the contacts between steel and aluminum because of their different thermal expansion coefficients. The main improvements in the optics in our third generation PFM are that the distance between objective lens and detection lens is kept constant, and the object's fine positioning is achieved with a xyz-piezo scanner. This ensures a fixed overlap between the trapping volume and the focus volume of the detection lens. Further improvements are, first, the use of a water immersion objective lens for trapping, which guarantees a space-invariant trap for distances up to 280 μm to the coverslip; second, spatial filtering of the signal at the PFM detector; and, third, a water dipping detection lens that enables micromanipulation in an open chamber.

Two nearly identical versions of this PFM have been set up in our laboratory at the European Molecular Biology Laboratory (EMBL). The main difference between the setups is that one is equipped with an acousto-optical modulator (AOM) and scan mirrors to control the intensity and position of the trapping laser.

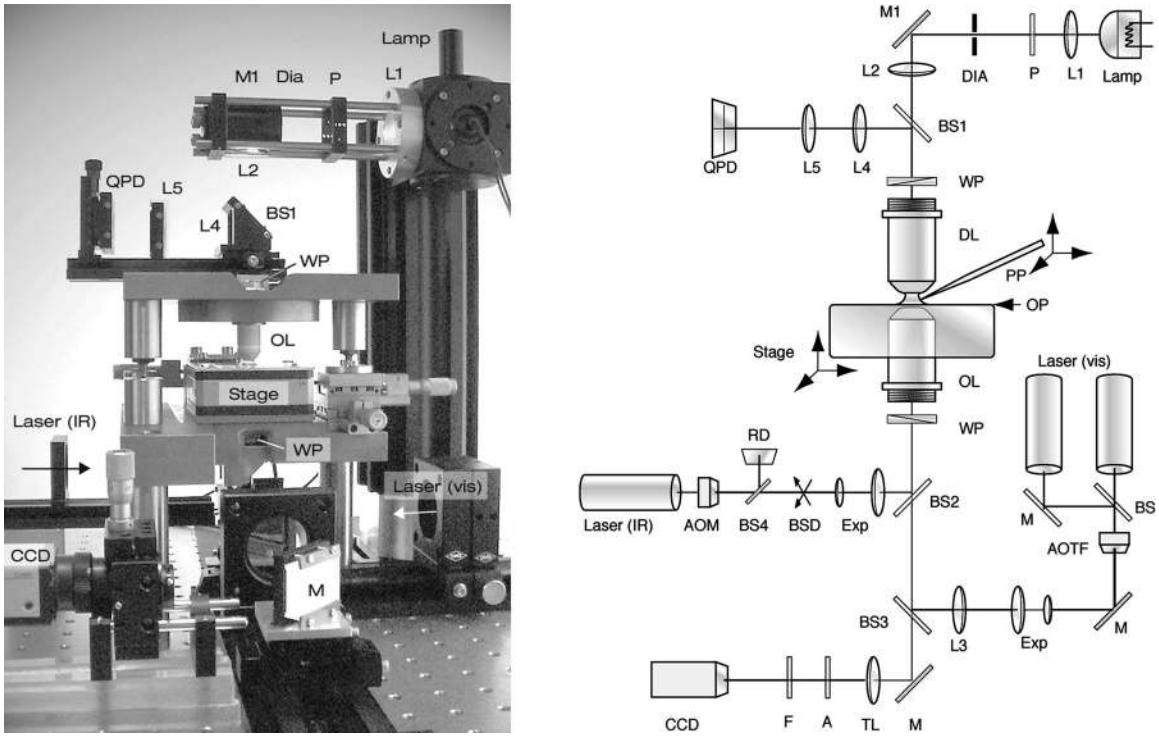

FIG. 3. Photo and schematic of a photonic force microscope. Light paths from three light sources (infrared laser, visible laser, and halogen lamp) pass several optical and mechanical elements: acousto-optical modulator (AOM), acousto-optical tunable filter (AOTF), beam steering device (BSD), reference diode (RD), beam expander (Exp), dichroic beam splitters (BS1–BS4), objective lens (OL), *xyz*-scan stage (stage), object plane (OP), patch pipette (PP), detection lens (DL), mirrors (M), lenses (L1–L5), quadrant photodiode (QPD), polarizer (P), diaphragm (Dia), Wollaston prisms (WP), analyzer (A), tube lens (TL), filter (F), and CCD camera (CCD).

A. PFM optics

The optics of the PFM can be split into an infrared (IR) trapping path and an infrared detection path, two visible illumination paths (fluorescence and bright field) and a visible detection path (see Fig. 3). For incoherent (Köhler) illumination or for differential interference contrast (DIC) a 100 W halogen lamp (lamp) is used, which is projected with a lens (L1) onto a diaphragm (Dia) after transmission through a polarizer (P). The lens (L2) can project the diaphragm into different positions in the back-focal plane of the DL by moving the mirror (M1). Off-axis illumination of the BFP permits oblique illumination in the object plane (OP). The detection lens (63× Achroplan, 0.9 water, 440069, Carl Zeiss, Germany) serves as a condensor. Two Wollaston prisms (WPs) in front of the detection lens and behind the objective lens (OL) allow the use of Nomarski type DIC. The 60× water immersion objective lens (UPLAPO60X/IR, Olympus, Japan) has a NA=1.2. The light emitted in the object plane passes the DIC analyzer (A) and a dual-band pass blocking filter (F) before a 180 mm tube lens (TL) forms an image on a charge coupled device (CCD) camera (Sony-Iris, Sony, Japan).

The coherent illumination path for fluorescence excitation consists of two gas lasers (vis) (visible emissions at 488 and 543 nm), which are controlled by an acoustooptic tunable filter (AOTF) (AA.AOTF.4C.T, Pegasus-Optik GmbH, Wallenhorst, Germany), expanded (Exp) and focused with a lens (L3) onto the BFP of the objective lens and provide wide field illumination over the whole field of view. Fluorescence is detected via the same path as transmitted (bright field) light. The beam splitter (BS3) is a dual-band pass dichroic filter, and BS2 is a short pass dichroic filter (all from AHF Analysentechnik, Tübingen, Germany).

The trapping laser (IR, 1064 nm) is an ultra low-noise (<0.03% intensity noise between 10 Hz and 10 MHz) diode-pumped Nd:YAG laser (IRCL-1000-1064-S, CrystaLaser, Reno, NV) with 1 W output power. An AOM (AA.MT.110/A1-IR, Pegasus-Optik GmbH, Wallenhorst, Germany) controls the power in the object plane. Eight percent of the light is deflected by BS4 onto a reference photodiode (RD) (S5107, Hamamatsu Photonics, Hamamatsu City, Japan), which records the intensity transmitted by the AOM. As a beam steering device (BSD) we use galvanometric scanning mirrors (M2, General Scanning Inc., Watertown, MA), which deflect the IR beam (at up to 1 kHz) with help of two scan lenses (not shown) at a variable angle onto the BFP of the objective lens. The IR beam is expanded twice (6× and 4×, 6× is not shown), which in combination with natural beam divergence results in twofold overillumination of the BFP ($w_0 = 2R = 14$ mm, w_0: Gauss waist, R: radius of lens aperture). The IR light focused by the objective lens is collected by the detection lens with $\mathrm{NA}_D = 0.9$ and a working distance of 1.46 mm. Two lenses (L4 and L5) with focal lengths of f_4 and f_5 project the BFP of the detection lens onto the QPD with magnification of f_5/f_4. Overillumination of the QPD enables spatial filtering by adjusting a detection angular aperture of $\sin(\alpha) < \mathrm{NA}_D/n_{\mathrm{water}}$ ($=0.9/1.33$) (see the aperture stop at the top in Fig. 2). The InGaAs PIN-QPD (G6849,

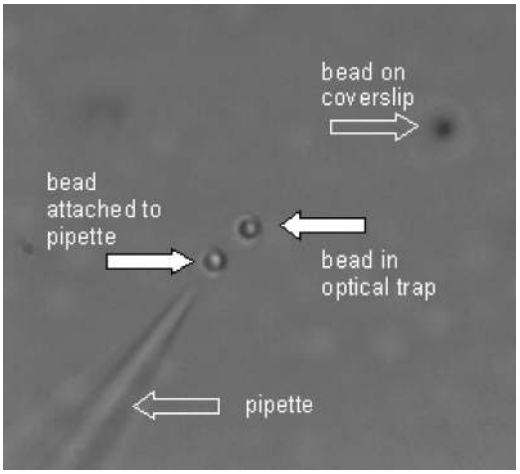

FIG. 4. Bright field image recorded in the photonic force microscope's object plane. Two latex beads with diameters of 1 μm each are held in the focal plane by the optical trap and by a micropipette, respectively. A third bead at the upper right is fixed out of focus on the coverslip.

Hamamatsu Photonics, Hamamatsu City, Japan) is 2.0 mm in diameter with a dead zone of 0.1 mm between quadrants. The photosensitivity is 0.67 A/W at 1064 nm and the cut-off frequency is about 20 MHz.

The locations and diameters of the BFPs of both the detection and the objective lens are important for the performance of the detection system. The BFP of the detection lens, with a diameter of 4.7 mm, is located inside its mounting -23.9 mm from the mounting thread. Therefore a conjugate image of the BFP must be formed at the QPD. The scanning mirrors, the BFP of the objective lens, the BFP of the detection lens, and the QPD are all at conjugate planes.

The objective lens has a transmission of 62% at 1064 nm wavelength and a working distance of 280 μm. The BFP of the objective lens, with a diameter of 7.2 mm, is -19 mm from the mounting thread. To estimate the laser power in the object plane we removed the objective lens and measured the power transmitted behind a 7.2 mm aperture stop with a thermosensitive laser power meter. The reference diode provided voltages proportional to the laser power. The laser powers measured were multiplied by the transmittance of the objective lens ($T=0.62$), leading to a maximum power of $P=80$ mW in the focus.

B. Piezo stage and micromanipulator

A specimen in the object plane can be moved coarsely along x and y with manual translation stages (461-XY-M, Newport GmbH, Darmstadt, Germany) and finely with a xyz-piezo scan table (Tritor 102 cap, piezosystem, Jena GmbH, Jena, Germany). The piezo scan table has 80 μm of travel along all three directions in closed loop mode, and 16 bit digital to analog (D/A) conversion leads to a minimum step size of about 1.2 nm. The patch pipette (PP) (a pulled glass capillary) is mounted on a xyz micromanipulator (M-313.80, XYZ, Physikalische Instrumente, Karlsruhe, Germany). Thus it is possible to suck a 1 μm bead and to move it relative to a probe held in the optical trap. The situation is shown in Fig. 4, where one bead is held by an optical trap, another by the PP in the focal plane, and a third bead is attached out of focus on the coverslip. For single molecule experiments the molecule can be tethered between the two beads in the focal plane. Figure 4 demonstrates the image quality obtained by oblique illumination of samples in the object plane. The image reveals a much better contrast for the beads than for the glass capillary at this scattering angle.

C. PFM electronics and software control

The electronics of the PFM are all controlled by software written in our laboratory. The software records the three detection signals of the QPD and that of the reference diode. Preamplification of the quadrant photodiode signals at 20 V/mA with 0.67 A/W photosensitivity leads to a voltage of 13.4 V/mW with a constant output noise of the preamplifier of 1 mV. Together with the main amplifiers (max 500×) the cut-off frequency of the amplification electronics (Öffner MSR-Technik, Plankstadt, Germany) is 1 MHz. A constant signal offset can be subtracted electronically, so that the result is digitized with a dynamic range of 12 bits. This is done for all four channels at up to 5 MHz per channel with a multifunction data acquisition (DAQ) PC card (NI 6110, National Instruments, Austin, Tx). The resulting three signal channels are displayed online with our PFM software. Pictures obtained at 25 Hz rate from the CCD camera are displayed with the help of a high-quality PC TV card. The xyz piezo table, the xyz micromanipulator, the scanmirrors, and the AOM for the IR laser are all computer controlled by our software. The signals for the scanning mirrors are DA converted with a high-quality PC sound card; the signal that controls the AOM is DA converted with the NI 6110 DAQ card.

D. Probes

The probes used for trapping are polystyrene (latex) microspheres with a refractive index of $n_s=1.57$ at $\lambda_0=1064$ nm. The beads, with 535 nm mean diameter, are nonfluorescent (Polybeads®, Polysciences, Inc., Warrington, PA). The microspheres, with mean diameters of 93 nm, 216 nm, and 1.03 μm, are fluorescence labeled (FluoSpheres®, Molecular Probes, Inc., Eugene, OR).

IV. DETECTION SYSTEM

Whereas in atomic force microscopy the transducer between sample and stage is mechanical (a cantilever), in photonic force microscopy the transducer (the trapped probe) is not in contact with the stage. The full three-dimensional position information of the probe in the trap is encoded in the interference of the scattered and unscattered light, which is recorded by the QPD. The principles behind the detection system (see Sec. II) and numbering of the quadrants are shown in Fig. 2, whereas all optical components are outlined in the schematic in Fig. 3.

A. Principles

The probe is displaced by the displacement vector $\mathbf{r}=(x,y,z)$ from the common geometric focus of the trapping lens and the detection lens. This alters the scattered field

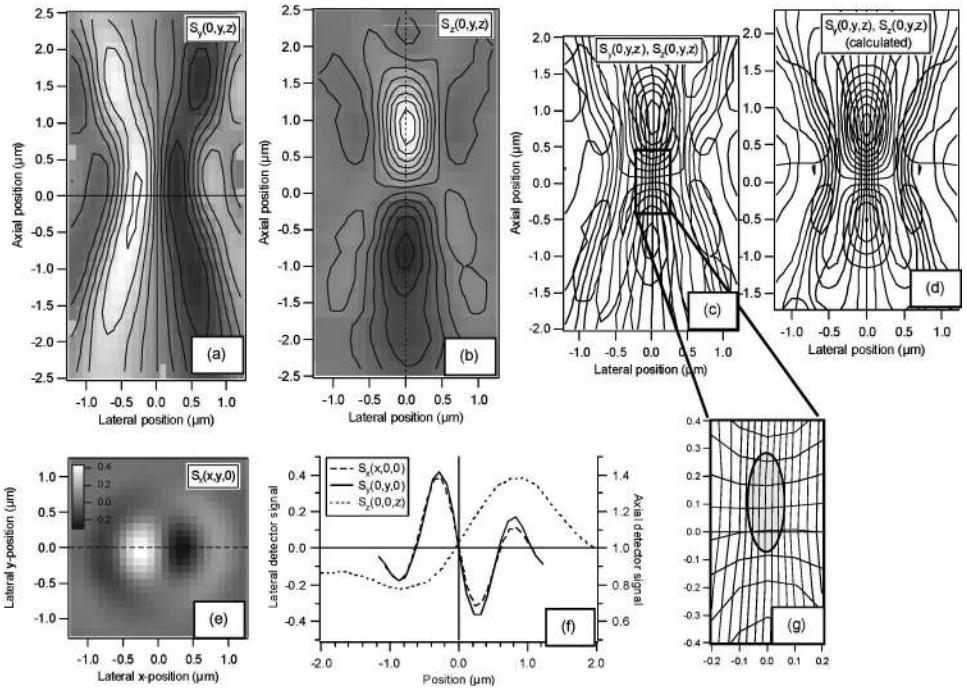

FIG. 5. Response (S_x, S_y, S_z) of the PFM-detection system for different positions of a 0.53 μm latex bead attached to a coverslip. Contour lines indicate constant signal intensities for different bead positions, dark (bright) gray levels indicate a negative (positive) detector signal. (a), (b) Signals $S_y(0,y,z)$ and $S_z(0,y,z)$ for bead displacements in the yz plane. (c), (d) Superposition of $S_y(0,y,z)$ and $S_z(0,y,z)$ for bead displacements in the yz plane (measured and calculated, respectively). The center region is magnified in (g) where vanishing curvature of the lines indicates that signals S_y and S_z are independent. The ellipsoid indicates a large trapping region. (e) Signal $S_x(x,y,0)$ for bead displacements in the xy plane. (f) Signal scans (S_x, S_y, S_z) along the three axes marked in (a), (b), and (e).

$\mathbf{E}_s(\mathbf{r}',\mathbf{r})$ in the focal plane and its Fourier transform $\tilde{\mathbf{E}}_s^+(K_x,K_y,\mathbf{r})$ in the back focal plane of the detection lens. The distribution in the BFP, i.e., the decomposition of a field into plane waves, is described by K vectors, $\mathbf{K}=[K_x,K_y,K_z=(K_x^2+K_y^2)^{1/2}]=k_0 n(\sin\varphi\sin\theta,\cos\varphi\sin\theta,\times\cos\theta)$. The angles (φ,θ) express the tilt of each plane wave relative to the optical axis. $k_0=2\pi/\lambda_0$ is the wave number in vacuum and n is the refractive index of the medium (e.g., water). The BFP of the detection lens has a diameter in K space, i.e., a width of the angular spectrum of $k_0\,\mathrm{NA}_D$ [$\mathrm{NA}_D=n\sin(\alpha_{\max})$ is the numerical aperture of the detection lens]. The incident field $\mathbf{E}_i(\mathbf{r}')$ and the forward scattered field $\mathbf{E}_s(\mathbf{r}',\mathbf{r})$ for a particle displaced by $\mathbf{r}$ in the FP become $\tilde{\mathbf{E}}_i(K_x,K_y)$ and $\tilde{\mathbf{E}}_s^+(K_x,K_y,\mathbf{r})$ in the BFP. Since both fields are coherent and interfere, the intensity at the QPD (which is in a conjugate plane of the BFP) is the modulus squared of the sum of both fields:

$$I_D(K_x,K_y,\mathbf{r})=\epsilon_0 c\left|\tilde{\mathbf{E}}_i(K_x,K_y)+\tilde{\mathbf{E}}_s^+(K_x,K_y,\mathbf{r})\right|^2 \times\mathrm{step}[k_0 n\sin(\alpha)-\sqrt{K_x^2+K_y^2}]. \quad (2)$$

The step function with radius $k_0 n\sin(\alpha)$ limits the angular aperture of the detection lens [$n\sin(\alpha)\leqslant\mathrm{NA}_D$]. For a detailed mathematical description see Ref. 42. $\sin(\alpha)$ can be adjusted by a diaphragm or by image magnification of f_5/f_4 with lenses L4 and L5 (see Fig. 3). With d_1 being the diameter of the BFP of the detection lens and $d_2<d_1$ the diameter of the QPD, the angular aperture can be adjusted to

$$\sin(\alpha)=(\mathrm{NA}_D/n)(d_2/d_1)(f_4/f_5). \quad (3)$$

The detection angular aperture $\sin(\alpha)$ determines the volume of the detection PSF and with it the overlap of the trapping volume. Furthermore $\sin(\alpha)$ determines the angular range of the wave that is captured by the detection lens and contributes to the signal at the QPD. Large $\sin(\alpha)$ can lead to a loss of signal sensitivity depending on the phase shift introduced by the particle itself.[43]

The intensity I_D in Eq. (2) is integrated over the area of each quadrant and delivers four intensity signals, $S_1(\mathbf{r},t)$ to $S_4(\mathbf{r},t)$. These are functions of the particle position $\mathbf{r}(t)$ and generate the signal triplet,

$$S[\mathbf{r}(t)]=(S_x,S_y,S_z) =[(S_1-S_2+S_3-S_4),(S_1+S_2-S_3-S_4), (S_1+S_2+S_3+S_4)]/S_0, \quad (4)$$

where S_0 is the unscattered intensity. Signals S_x and S_y are obtained from the differences in the left and right quadrant signals and the upper and lower quadrant signals, respectively. S_x and S_y measure the lateral modulation $\exp(-iK_x x-iK_y y)=\exp[-i\Delta\phi(x)-i\Delta\phi(y)]$ of the scattered field relative to the unscattered field. The signal S_z is a sum signal that varies linearly with small axial particle displacement z due to the phase difference $\Delta\phi(z)$ between the scattered and the unscattered fields. Although the dielectric particle scatters light with constant phase delay of $\pi/2$, the phase difference $\Delta\phi(z)$ some wavelengths behind the focus depends explicitly on the z position. The reason for that is the Guoy phase shift (phase anomaly)[44,45] inherent in every (nonplane) wave that leads to a π phase shift over the distance of the axial

focus extension. Remarkably, the mean wavelength in the focus is increased and the mean momentum vector **K** is decreased compared to a plane-wave reference.

The signal triplet in Eq. (4) was measured for different positions **r** of a 0.53 μm latex bead fixed on a coverslip and was moved by the piezo stage in the xy, the xz, and the yz planes. The results are shown in Figs. 5(a), 5(b), and 5(e) for the signals $S_y(0,y,z)$, $S_z(0,y,z)$, and $S_x(x,y,0)$. Displacements **r** are shown over a range that is much wider than that explored by a probe in an optical trap. Bright/dark gray values indicate positive/negative signals for S_x and S_y, and signals larger/smaller than 1 for S_z. Contour lines indicate constant signals for different positions **r**. Overlays of the contour lines of $S_y(0,y,z)$ and $S_z(0,y,z)$ in Figs. 5(c), 5(d), and 5(g) reveal that in the central trapping region the lines are nearly straight and orthogonal, showing the linearity and independence of the signals. This is not the case for larger displacements. Linearity is also bared in Fig. 5(f) where line scans through the center of focus at $\mathbf{r}=(0,0,0)$ are plotted. Figure 5(d) is the theoretical detector response and corresponds to Fig. 5(c). In the experiments we found a linear detection range of 1/2–3/4λ in the axial direction and about 1/4–1/2λ in lateral direction depending on the size of the sphere ($\lambda = 1064$ nm/1.33). We assume for the water immersion trapping lens that the detector response of a dielectric bead on a coverslip is the same as that of a bead that diffuses in an optical trap. This assumption was consolidated by a novel study[46] where the detector response is determined by the fast (and linear) diffusion of a trapped particle.

B. Three-dimensional scan paths

To demonstrate the performance of the PFM detection system we moved a 0.53 μm latex bead attached to a coverslip along three-dimensional paths through the optical focus and recorded the signals with the QPD in the manner described above. The minimum addressable step size of the piezo stage, $\Delta r = 1.2$ nm (which is 0.0015 λ with $\lambda = 1064$ nm/1.33), was used to move the bead between positions. One hundred position signals $\mathbf{S}'(\mathbf{r})$ (the prime indicates that the signal is not normalized by S_0) were recorded and averaged for 0.1 s at each position. Figure 6(a) displays two parametric representations of the signals measured, $S'_x[\mathbf{r}(t)]$, $S'_y[\mathbf{r}(t)]$, and $S'_z[\mathbf{r}(t)]$, for two cubic paths with 12 and 48 nm edge lengths, whereas Fig. 6(b) displays the same signals, $S'_x(t)$, $S'_y(t)$, and $S'_z(t)$, for the large cubic path. Only every fourth point is indicated by a symbol for the sake of clarity. Slow variations in the signal intensity (0.01–10 Hz) in Fig. 6(b) due to air circulating and slight intensity instability of the trapping laser (at <10 Hz) led to the effect that the parametric representations of the scan paths (the cubes) are not completely closed (gaps <10 nm). This is shown in Fig. 6(a). The detection system can be improved further by adding a feedback control for the AOM.

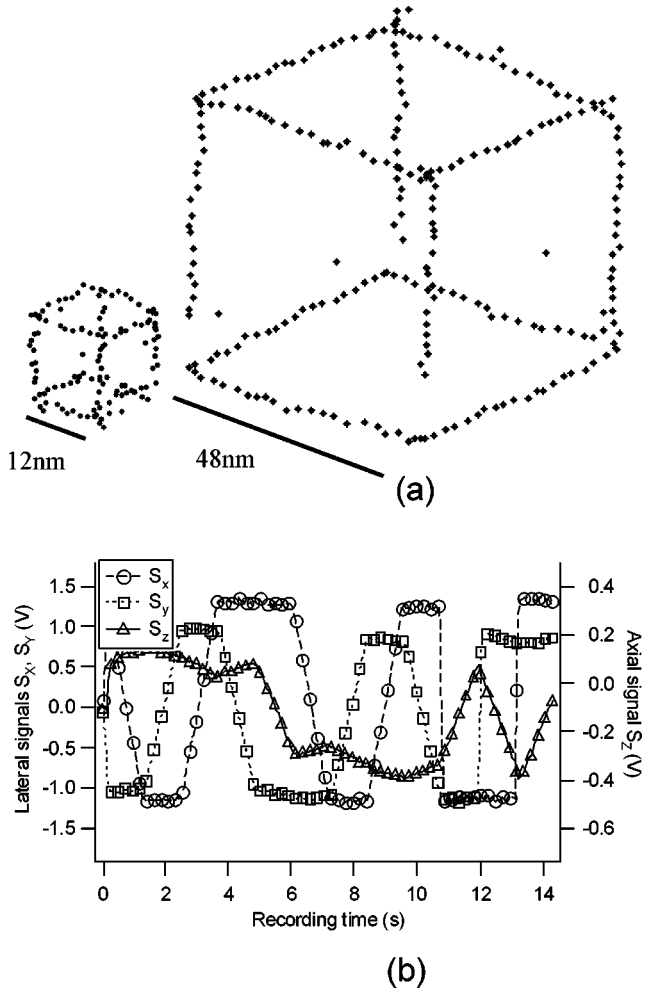

FIG. 6. (a) Two three-dimensional particle tracks of a 0.53 μm latex bead attached to a coverslip. The piezo stage moved the bead along a path, which constitutes a cube through the focus. The PFM-detection system recorded the center positions of the bead, which are represented by black dots. The step size was 1.2 nm. (b) Parametric representation of the three detection signals for the larger cube over a recording time of ~ 14 s (~ 8 s for the small cube).

V. SYSTEM NOISE

Noise inherent in a measurement system limits the resolution, precision, and sensitivity of experiments. It is therefore indispensable to investigate and quantify the system noise and to consider it during data analysis. The system noise in the PFM due to mechanical vibrations, laser instability, and induced electronic noise can be measured with the PFM detection system and a probe tightly coupled to the stage. It is thereby possible to distinguish between lateral and axial vibrations transferred to the probe. While fluctuations of mechanical origin produce signals in x, y, and z, instability of the laser and/or the AOM results only in z signals. We attached a 0.53 μm bead tightly to a coverslip by adding phosphate buffered soline (PBS), which diminishes electrostatic repulsion between the glass surface and the latex bead. This enables the bead to touch the surface so that attractive van der Waals forces bind the bead to the coverslip. By holding the bead in the center of the trapping focus, even tiny displacements of the bead can be recorded by the QPD. We measured the x, y, and z signals, $S'_x(t)$, $S'_y(t)$, and $S'_z(t)$ (in volts, the prime indicates that the signals are not normalized by S_0) for 5 s at 1 MHz sampling frequency, and determined the power spectral density (PSD) (in units of V^2 s), which are the modulus squares of the Fourier transform of the signals

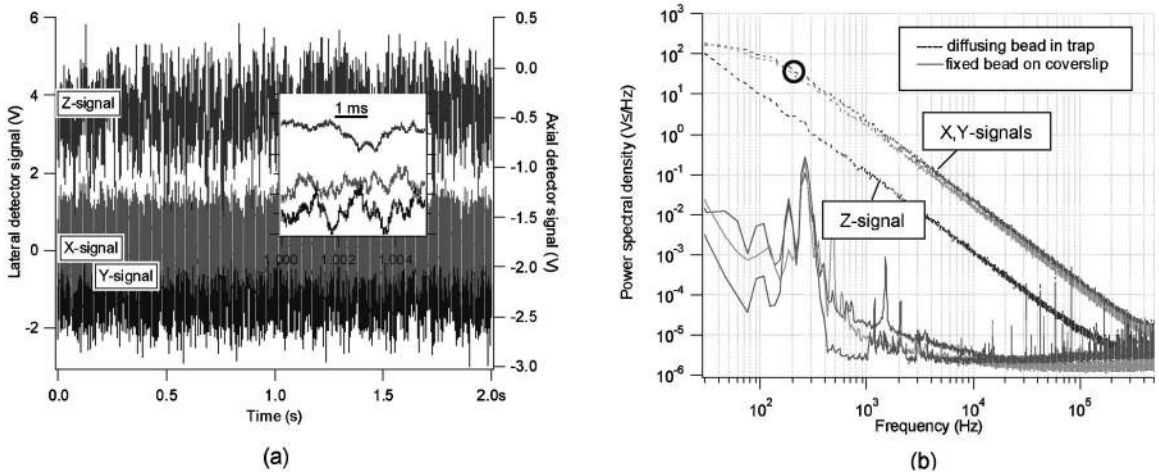

FIG. 7. (a) Detector signals $S_x'(t)$, $S_y'(t)$, and $S_z'(t)$ as raw data (voltages) of a trapped 0.53 μm latex bead. The inset shows a short time period of 5 ms that resolves the fast fluctuations of the bead at a rate of 1 MHz. (b) Power spectral density of the signals $S_x'(t)$, $S_y'(t)$, and $S_z'(t)$ of a bead diffusing in the trap (three dotted lines). The black circle indicates the corner frequencies at 3 dB of the lateral power spectra. A 0.53 μm bead fixed on the coverslip reveals low noise in the PFM mainly below 2 kHz (three solid lines).

$S(t)'$. The PSDs are plotted in Fig. 7 for a bead moving freely in the optical trap and for a bead fixed on the coverslip. The fixed bead vibrated slightly relative to the center of the focus especially at frequencies of about 200 and 300 Hz, which are the resonance frequencies for axial and lateral translations of the piezo scan stage. For all other frequencies (50 Hz–50 kHz) the background noise is three to five orders of magnitude smaller than the fluctuation signals of the bead in the optical trap. The lateral signals are still clearly above the noise level at the maximum signal frequency of 0.5 MHz, whereas the z signal disappears in the noise at about 300 kHz. Here the signal-to-noise ratio is 1 and the particle position cannot be determined at this frequency. The single line noise peaks at high frequencies are aliasing effects generated by the discrete Fourier transforms used to obtain the PSDs. However, after calibration of the detector, the standard deviations of the fluctuations of the fixed bead are $(\delta x, \delta y, \delta z) = (0.7,\ 2.1,\ 2.1)$ nm over the whole range of frequency. Application of a high pass filter at 2 kHz reduces the fluctuations to $(\delta x, \delta y, \delta z) = (0.15,\ 0.17,\ 0.54)$ nm. $(\delta x, \delta y, \delta z)$ are the smallest measurable displacements of a 0.53 μm bead, which is either slowly positioned or fluctuates in solution at rates >2 kHz. The bead displacements along the paths in Fig. 6 were averaged over 100 positions per point at a sampling rate of 1 kHz, thus leading to well-determined, straight lines along the edges of the cube. We have not found any study which reports comparably small values for the stability of an optical trapping system.

The performance limit of the detector due to electronic noise can be estimated by considering the scattering strength or efficiency Q_{sca} of a particle. For a 0.53 μm latex bead $Q_{\mathrm{sca}} = 22\%$ of the photons "hitting" the sphere are scattered. Mean axial sensitivity of 57%/μm for this scatterer can be read in Fig. 5(f). We further assume that a laser power of 0.3 mW reaches the quadrant photodiode. Preamplification provides a voltage of 0.3 mW·13.4 V/mW=4.0 V (see also Sec. III C). A change of 57%/μm results in 2.28 V/μm. The voltage floor due to preamplifier noise is 1 mV, hence the axial resolution limit due to this noise is 1 μm/2280=0.4 nm. The lateral resolution limit is even smaller due to the higher detector sensitivity [see the slopes in Fig. 5(f)].

VI. TRAPPING SYSTEM

The main task of the trapping system is to confine the fluctuations of the probe to a specific volume. This trapping volume is tuned in size by the laser power and in shape by the optical system (objective lens and spatial filters), i.e., it can be adjusted to the experimental condition. The balance of optical forces that act on a probe needs to be well characterized by a precise calibration of the optical trap before external forces acting on the probe can be measured. The trapping stability and visibility of a particle influence the feasibility of an experiment.

A. Optical forces

The optical force $\mathbf{F}_{\mathrm{opt}}(\mathbf{r}) = \boldsymbol{k}(\mathbf{r} - \mathbf{r}_0)$ introduced in Eq. (1) can be approximated as a linear function in all three directions provided displacement $|\mathbf{r} - \mathbf{r}_0|$ is small. Along the x, y, and z axes the forces are on average $F_x = k_x x$, $F_y = k_y y$, $F_z = k_z(z - z_0)$, where k_x, k_y, and k_z are the diagonal elements of the stiffness matrix $\boldsymbol{k}$, i.e., the mean stiffnesses along x, y, and z. However, for larger displacements or for special focal intensity distributions, the optical force becomes highly nonlinear. It is convenient to split the total optical force on a particle into two components, the gradient and the scattering force, $\mathbf{F}_{\mathrm{grad}}(\mathbf{r})$ and $\mathbf{F}_{\mathrm{sca}}(\mathbf{r})$:[47]

$$\mathbf{F}(\mathbf{r}) = \mathbf{F}_{\mathrm{grad}}(\mathbf{r}) + \mathbf{F}_{\mathrm{sca}}(\mathbf{r}) = \int_V \int \int \frac{\alpha n_m}{2c} \nabla I_i(\mathbf{r}')\, dV' + \frac{n_m}{c} I_0 \cdot C_{\mathrm{sca}}(\mathbf{G}/K_n). \quad (5)$$

The gradient force $\mathbf{F}_{\mathrm{grad}}$ is the sum of all dipole forces that act on different dipole volume elements inside the scatterer and pull each element along the intensity gradient. $\nabla I_i(\mathbf{r}')$ is the gradient of the intensity for a volume element at $\mathbf{r}'$ inside the scatterer. For a particle with a diameter smaller than the wavelength and a refractive index not much larger than unity,

the Born approximation (Rayleigh–Gans approximation) is valid and the (nonconstant) intensity distribution inside the particle is proportional to the distribution without scatterer $\nabla I_i(\mathbf{r}') \propto \nabla I_{\text{internal}}(\mathbf{r}')$. The polarizability α is a function of the refractive indices n_m and n_s outside and inside the scatterer. c is the speed of light in vacuum. The scattering force $\mathbf{F}_{\text{sca}}$ is the sum of all changes of the Poynting vector, i.e., of the momentum vector $\hbar\boldsymbol{K}$ due to scattering at the particle. The transfer vector $\mathbf{G}$ points in the direction of mean momentum transfer, which is the z direction for spheres located on axis in symmetric incident fields. The magnitude $|\mathbf{G}/K_n| = |\langle\cos(\theta_i)\rangle - \langle\cos(\theta_s)\rangle|$ is obtained by the difference in the mean $\mathbf{K}$-direction cosines from the incident and the scattered field.[47] The power of the scattered light $I_0 C_{\text{sca}}$ is defined by the intensity in the focus of the incident beam, $I_0 = \epsilon_0 c|\mathbf{E}_i(0,0,0)|^2$. The scattering cross section C_{sca} (Ref. 48) is computed from the scattered intensity $|\tilde{\mathbf{E}}_s^{\pm}(\boldsymbol{K}_x, \boldsymbol{K}_y, \mathbf{r})|^2$. The scattering force is especially pronounced in the z direction and is always positive for particles smaller than the wavelength and with refractive index $n_s > n_m$ (n_m is the index of the surrounding medium). The region in which stable trapping occurs (neglecting thermal noise) is where the gradient force outbalances the scattering force, i.e., $|\mathbf{F}_{\text{grad}}(\mathbf{r})| = |\mathbf{F}_{\text{sca}}(\mathbf{r})|$. A quasiray-optical study for particles larger than the wavelength (Mie scatterers) can be found in Ref. 49 or 50.

B. Exploring the trapping volume

The Langevin equation presented in Eq. (1) describes the stochastic movement of a particle influenced by optical (trapping) forces. For small particle displacements $(\mathbf{r}-\mathbf{r}_0)$ from the trap center $\mathbf{r}_0=(0,0,z_0)$ the optical trapping force $\mathbf{F}_{\text{opt}}(\mathbf{r}) \approx [k_x x, k_y y, k_z(z-z_0)]$ is not only linear with displacement $\mathbf{r}$, but it is also nearly conservative. It can be shown by Brownian dynamics simulations that the fraction of the nonconservative force vanishes for small displacements in ideal optical traps. Therefore, thermodynamic equilibrium of the particle with the environment is ensured, allowing the application of Boltzmann statistics;

$$p_B(\mathbf{r}) = p_0 \exp\left(-\frac{W(\mathbf{r})}{k_B T/2}\right) \approx p_0 \exp\left(-\frac{k_x x^2}{k_B T} - \frac{k_y y^2}{k_B T} - \frac{k_z z^2}{k_B T}\right), \tag{6}$$

$$W(\mathbf{r}) = -k_B T \ln[p_B(\mathbf{r})] + W_0 \Leftrightarrow \mathbf{F}(\mathbf{r}) = -k_B T \frac{\nabla[p_B(\mathbf{r})]}{p_B(\mathbf{r})}. \tag{7}$$

$p_B(\mathbf{r})$ is the three-dimensional probability density of finding a particle in a potential $W(\mathbf{r}) = -\int \mathbf{F}_{\text{opt}}(\mathbf{r})\mathbf{dr}$ at position $\mathbf{r}$ and temperature T, the parameter p_0 normalizes $\int p_B(\mathbf{r}) d^3 r$ to 1, and thus $W_0 = k_B T \ln(p_0)$. Due to the linearity of the force $\mathbf{F}_{\text{opt}}(\mathbf{r})$, the trapping potential $W(\mathbf{r})$ is harmonic in all directions as expressed in Eqs. (6) and (7). Figures 8 and 9 display both projected 2D position histograms (top four graphs) and projections of the corresponding trapping potentials along lines through the trap center (lower two graphs). A total of 1 000 000 bead center positions were recorded for each plot at a sampling rate of 500 kHz. The particle explores the trapping volume, which is larger for smaller optical forces.

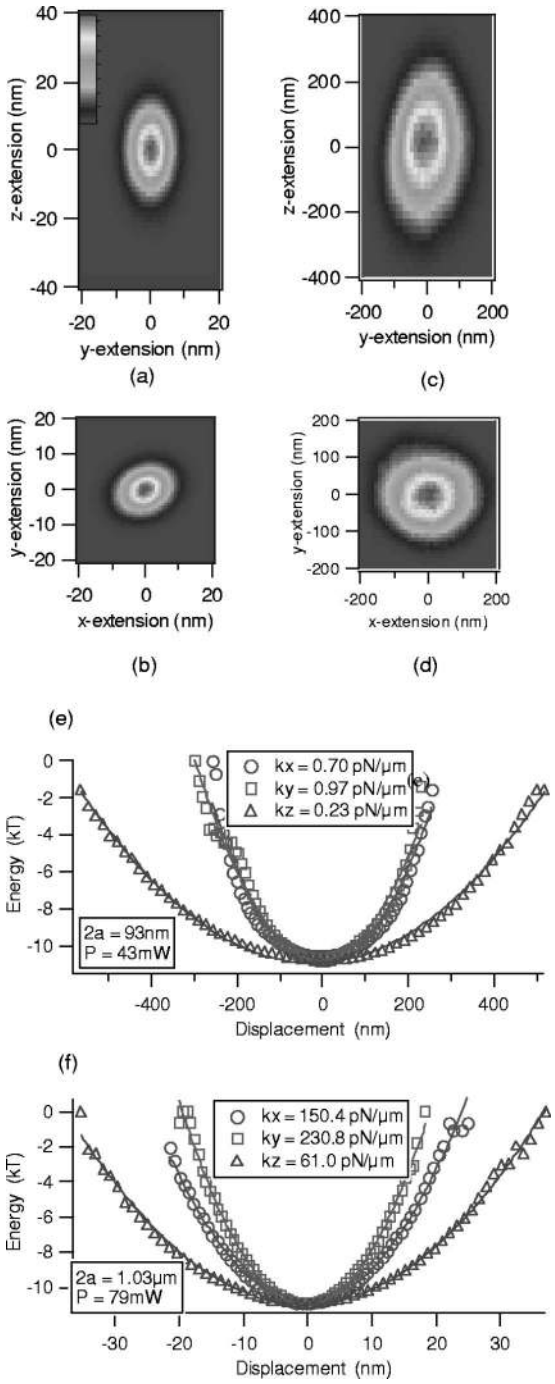

FIG. 8. 2D histograms of bead center positions and line profiles of the trapping potentials. The upper and lower histograms of bead positions inside the trap are projections along the x and z axes, respectively. (a), (b) Extent of the small trapping volume of a 1.03 μm latex bead trapped with a laser power of $P=79$ mW. (c), (d) Large trapping volume of a 93 nm latex bead at $P=43$ mW. Note the different scales of the axes. (e), (f) Projections of the trapping potential along x, y, and z, showing that the optical trap is harmonic in all three directions. The axial stiffness $k_z=0.23$ pN/μm of the 93 nm bead is three orders of magnitude smaller than the lateral stiffness $k_y=230$ pN/μm of the 1.03 μm bead

Figures 8 and 9 show both the position distributions of the maximum achievable trapping force [Figs. 8(a) and 8(b) and 9(a) and 9(b)] and those of a very small force [Figs. 8(c)

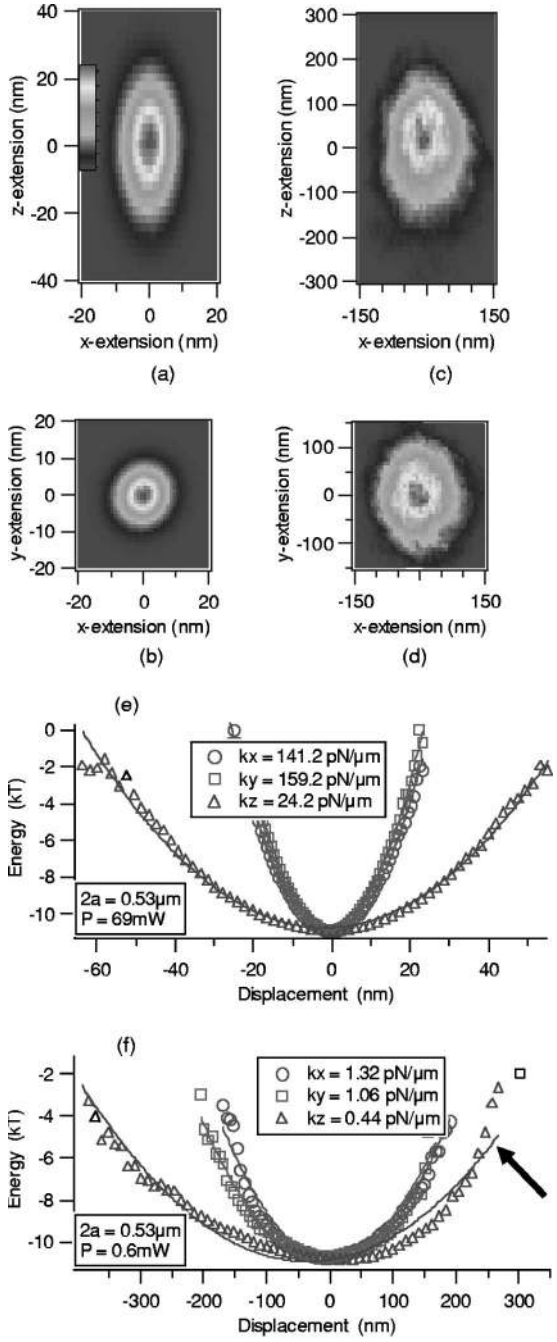

FIG. 9. 2D histograms of bead center positions and line profiles of the trapping potentials. (a), (b) Extent of the small trapping volume of a 0.53 μm latex bead trapped with a laser power of $P=69$ mW in the focal plane. (c), (d) Large trapping volume of the same bead at $P=0.6$ mW. Note the different scales of the axes. (e), (f) The optical trapping potential profiles are harmonic along x, y and z. Only the axial profile at $P=0.6$ mW shows small buckling for large positive displacements (shown by the arrow).

and 8(d) and 9(c) and 9(d)]. In Fig. 8 two different bead sizes were used. A 1.03 μm latex bead was trapped at a nominal laser power of $P=79$ mW in the focal plane, resulting in a trapping volume cross section of about 30×15 nm [at $p_B(\mathbf{r})=p_B(\mathbf{r}_0)/e$] and a 0.09 μm latex bead at $P=43$ mW, resulting in a trapping volume cross section of about 400×200 nm. The upper two histograms [Figs. 8(a) and 8(c)] are projections in the yz plane, and the lower two histograms [Figs. 8(b) and 8(d)] are projections in the xy plane and reveal the asymmetry of the trap due to linearly x-polarized light. The corresponding trapping potentials are obtained by taking the logarithm of $p_B(\mathbf{r})$ described by Eq. (6).

Projections of these potentials in the x, y, and z axes are plotted below the histograms and show the harmonic behavior of the trapping potentials. For all trapping forces, the maximum thermal energy accumulated by the particle is about $10k_BT$ although the average thermal energy of a freely diffusing particle is only $3/2k_BT$. For the optical trap of the small particle an axial trap stiffness k_z of only 0.23 pN/μm was measured, whereas the lateral trap stiffness k_y for the larger bead is three orders of magnitude higher (230 pN/μm). The results shown in Fig. 9 are for a 0.53 μm latex bead, which was first trapped at a laser power of $P=69$ mW and then at $P=0.6$ mW. The cross section of the stronger trap is about 40×15 nm, that of the weak trap is about 300×150 nm [at $p_B(\mathbf{r})=p_B(\mathbf{r}_0)/e$]. However, both the 2D-position histogram and the potential line scan reveal an asymmetry especially along the z direction, which is an artifact of the detection system. Since the 0.53 μm bead is trapped behind the center of the focus and explores a large volume, the phase difference of the scattered and the unscattered field becomes nonlinear with large axial particle displacements and reaches a maximum of intensity at $z\approx1$ μm [see Figs. 5(b), 5(c), and 5(f)]. As a result the position histogram in Fig. 9 is cut off in the positive z direction and the corresponding potential seems to buckle and become nonharmonic. This effect, predicted by a recent theoretical study[43] and now confirmed experimentally, becomes stronger for small laser powers and for increasing bead diameter and refractive index.

Three-dimensional Gaussian distributions $p_{\text{trap}}(\mathbf{r})$ result from a freely diffusing probe inside the trap. Any interaction of the probe due to conservative external forces $\mathbf{F}_{\text{ext}}$ (or structures) results in an external interaction potential W_{ext}, which adds to the trapping potential W_{trap} (see the schematic in Fig. 1). This is valid if $\mathbf{F}_{\text{ext}}$ does not result in a change of the electric field in the focus. Then the resulting histogram $p_B(\mathbf{r})$ is a product of the original distribution $p_{\text{trap}}(\mathbf{r})$ with the Boltzmann distribution $p_{\text{ext}}(\mathbf{r})$ from the external interaction,

$$p_B(\mathbf{r})=p_0\exp\left(-\frac{W_{\text{trap}}(\mathbf{r})+W_{\text{ext}}(\mathbf{r})}{k_BT/2}\right)=p_{\text{trap}}(\mathbf{r})p_{\text{ext}}(\mathbf{r}). \quad (8)$$

A simple case of an external interaction potential W_{ext} can be generated by introducing an interface that intersects the trapping volume and repels the bead due to electrostatic forces. This principle is illustrated in Fig. 10, where a 0.53 μm bead approaches the coverslip. The optical trap holding the fluctuating bead was moved in 0.4 μm steps towards the interface, leading to a significant change in the position signal histograms as can be seen in the top row of Fig. 10. The trapping volume is diminished by the presence of the coverslip, because the bead center cannot approach closer to the interface than the bead radius (indicated by the particle center track). However, the change in the distribution $p_B(\mathbf{r})$ near the coverslip includes other, more complicated effects in addition to the electrostatic repulsion of the bead. These include the direction dependent increase of the viscous drag,[24]

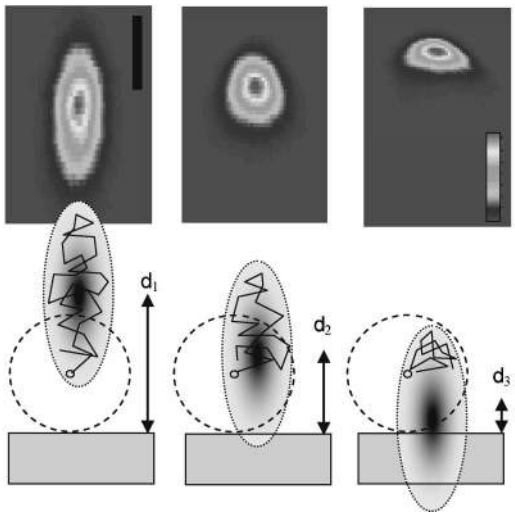

FIG. 10. Bead position histograms for different distances d of the beam focus center to the coverslip. The histograms of measured center positions (top row) are projections into the xz plane. The bar in the first histogram indicates an extent of 100 nm. The coverslip at the bottom is shown as a gray bar. The bead outlined is shown by a dashed line and the centers of the respective foci (shown as ellipsoids) have distances of d_1, $d_2=d_1-0.4\ \mu$m, $d_3=d_1-0.8\ \mu$m to the interface. Possible bead center tracks are outlined inside the foci. The bead diameter was 0.53 μm, and the laser power was 7 mW.

van der Waals attraction by the interface and, last but not least, the nonlinearity of the detection system.

In a recent study Clapp and Dickinson[38] measured the surface forces on a silica sphere close to a coverslip with optical tweezers. With the help of an evanescent the wave axial Brownian fluctuations of the trapped particle were measured to determine the axial trap stiffness as a function of the axial distance to the trap. From these it was possible to deduce the surface interaction potentials. In contrast to our technique, they used thermal fluctuations exclusively to calibrate the optical trap.

C. Comparison between theory and experiment

The deficiency in common electromagnetic theories for optical trapping forces is either due to an inaccurate description of the incident electromagnetic field[51,52] or a restriction in size.[47,53,54] However, optical forces can be calculated correctly for sphere sizes up to the laser wavelength λ_0/n (Refs. 40 and 47) by solving the vectorial Helmholtz equation without paraxial approximations. It is essential to consider the overillumination of the objective lens' BFP (circular aperture with radius R) by a Gaussian beam with waist w_0, as well as the effect of an aplanatic lens (sine condition), and, if present, the phase changes due to interfaces. For our experiments the laser power in the focus was measured, described in Sec. III A, and the concentric overillumination of the Gaussian beam ($w_0=2R$) and the planarity of the phase at the BFP were carefully confirmed. As probes we used latex beads with mean diameters of nominally 535 (nonfluorescent) and 216 nm (fluorescent), which can be both categorized as Rayleigh–Gans scatterers.[48] A bead of each size was held in the optical trap, while the laser power was decreased stepwise after recording 400 000 bead positions each for high laser powers and 800 000 positions for lower laser powers. The sampling rate was 200 kHz. The average trap stiffnesses k_x, k_y, and k_z were determined for the x, y, and z directions as described in our discussion on noise analysis. The resulting dependence of the three force constants on the laser power is plotted by solid lines in Fig. 11 for the 0.53 μm bead on the left and for the 0.22 μm bead on the right. The calculated results are plotted by dashed lines and were taken from a recent study (see the table in Ref. 42). The calculated distribution of optical forces $\mathbf{F}_{\mathrm{opt}}(\mathbf{r})$ was used to perform Brownian dynamics simulation according to Eq. (1) (with $\mathbf{F}_{\mathrm{ext}}=0$) to generate the position distributions $\mathbf{r}(t)$ and the corresponding signal distributions $\mathbf{S}[\mathbf{r}(t)]$. The latter were then fed into our noise analysis software (also used for the experiments), which generates weighted averages of all force constants inside the trapping volume along x, y, and z.

VII. NOISE ANALYSIS AND SYSTEM CALIBRATION

For quantitative measurements it is necessary to calibrate both the optical trap and the detection system. This means that both the usually linear relation between optical

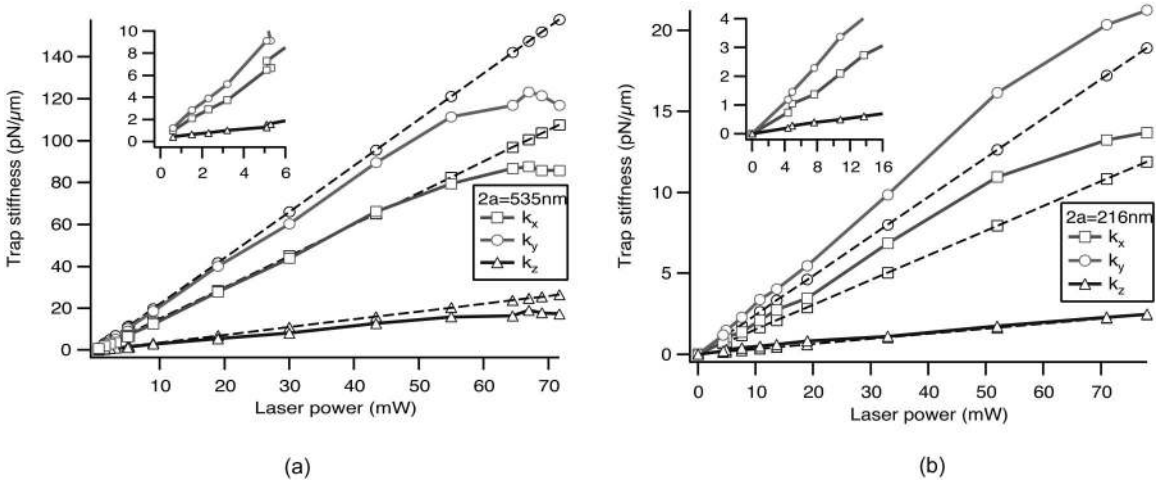

FIG. 11. Trap stiffnesses (force constants) k_x, k_y, and k_z along x, y, and z as a function of the laser power. The electric field in the focus was linearly polarized in the x direction, thus leading to a stiffer trap along y. The solid curves represent experimental data, the dashed lines correspond to calculated trap stiffnesses. The insets show the dependence of the trap stiffnesses on small laser powers. (a) Trap stiffnesses of a 535 nm latex bead. (b) Trap stiffnesses of a nominally 216 nm latex bead.

force $\mathbf{F}(\mathbf{r})$ and particle displacement $\mathbf{r}$ and between detector signal $\mathbf{S}(\mathbf{r})$ and displacement $\mathbf{r}$ has to be determined. Although various calibration techniques are suitable,[55] the so-called Langevin method emerged as the most flexible and the easiest to apply.

The linearity approximations $\mathbf{F}(\mathbf{r}) \approx \boldsymbol{k} \cdot \mathbf{r}$ and $\mathbf{S}(\mathbf{r}) \approx \boldsymbol{g} \cdot \mathbf{r}$ and the assumption that both the forces and the signals are orthogonal in x, y, and z require that $\boldsymbol{k}$ and $\boldsymbol{g}$ are diagonal matrices such that $\mathbf{F}(\mathbf{r}) = \boldsymbol{k}[\boldsymbol{g}^{-1}\mathbf{S}(\mathbf{r})]$, where $\boldsymbol{g}^{-1}$ is the inverse matrix of $\mathbf{g}$. Matrix $\mathbf{k}$ has diagonal elements k_x, k_y, and k_z (trap stiffnesses in x, y, and z) and regards the natural asymmetry of the optical trap. $\boldsymbol{g}$ is approximated by a diagonal matrix with elements g_x, g_y, and g_z (detector sensitivities in x, y, and z). The viscous drag $\boldsymbol{\gamma}(\mathbf{r})$ is a matrix too. Under these assumptions the Langevin equation for the detector signals $\mathbf{S}[\mathbf{r}(t)] \approx \mathbf{S}(t)$ [see Eq. (1)] without external forces reduces to

$$\boldsymbol{g}^{-1}(m \cdot \ddot{\mathbf{S}}(t) + \boldsymbol{\gamma} \cdot \dot{\mathbf{S}}(t) + \boldsymbol{k} \cdot \mathbf{S}(t)) = \mathbf{F}_{\mathrm{th}}(t). \tag{9}$$

The time average of the random force $\langle \mathbf{F}_{\mathrm{th}}(t) \rangle = 0$ disappears and its autocorrelation is described by a δ function,

$$\langle \mathbf{F}_{\mathrm{th}}(t) \mathbf{F}_{\mathrm{th}}(t+\tau) \rangle = 2M\gamma k_B T \delta(\tau), \tag{10}$$

when the sampling time is longer than the time between two collisions, which is usually the case. M is the number of dimensions. The Fourier transform of Eq. (10) is the force spectral density $|\tilde{F}_{\mathrm{th}}|^2 = M\gamma k_B T/\pi$ in units of N^2 s. The Fourier transform of Eq. (9) is

$$\boldsymbol{g}^{-1}(-m\omega^2 + i\gamma\omega + \boldsymbol{k})\tilde{\mathbf{S}}(\omega) = \tilde{\mathbf{F}}_{\mathrm{th}}(\omega). \tag{11}$$

Then the power spectral density PSD of the particle position signal S_i $(i = x,y,z)$ for a harmonic potential $-\int F_i dx_i = k_i/2(S_i/g_i)^2$ is given by[56]

$$|\tilde{\mathbf{S}}_i(\omega)|^2 = \frac{\gamma k_B T/(\pi g_i^2)}{(k_i - m\omega^2)^2 + \gamma^2\omega^2} \approx \frac{D/(\pi g_i^2)}{\omega_i^2 + \omega^2}. \tag{12}$$

D is the diffusion constant, defined by the Einstein relation $D = k_B T/\gamma$. The PSD is described by a Lorentz curve with characteristic frequency $\omega_i = k_i/\gamma$ [see the double logarithmic plot in Fig. 7(b)] and reduces for small particle masses $m \ll \gamma/\omega = \gamma\tau$ (Ref. 57) to $|\tilde{x}_i(\omega)|^2 = |\tilde{S}_i(\omega)/g_i|^2 = D/(\omega^2\pi)$ in direction x_i when the optical force is zero, i.e., $k_i = 0$.

The inverse Fourier transform of the PSD in Eq. (12) is the autocorrelation function $\langle S_i(t) S_i(t+\tau) \rangle$ and is an exponential,

$$\langle S_i(t) S_i(t+\tau) \rangle / g_i^2 = \langle x_i(t) x_i(t+\tau) \rangle = k_B T/k_i \exp(-\tau \cdot k_i/\gamma). \tag{13}$$

For a freely diffusing particle and for sampling times $\tau \gg m/\gamma$, the autocorrelation approaches a δ function, i.e., $\langle x_i(t) x_i(t+\tau) \rangle = 2D\delta(\tau)$.

In the experiment only the fluctuations of the position signal $S_i'(t)$ (measured in volts) are recorded. The histograms of position signals $p_B[S_i'(\mathbf{r})]$ provide the widths σ_i' of these Gaussian distributions in direction x_i. An optical trap can be calibrated along direction x_i by fitting a Lorentz function to the PSD $|\tilde{S}_i'(\omega)|^2$ according to Eq. (12) to determine the trap stiffness $k_i = \gamma\omega_i$ via the corner frequency ω_i [see the circle in Fig. 7(b)]. Alternatively $k_i = \gamma/\tau_i$ can be obtained via the autocorrelation time τ_i by fitting an exponential to the autocorrelation $\langle S_i'(t) S_i'(t+\tau) \rangle$ according to Eq. (13).

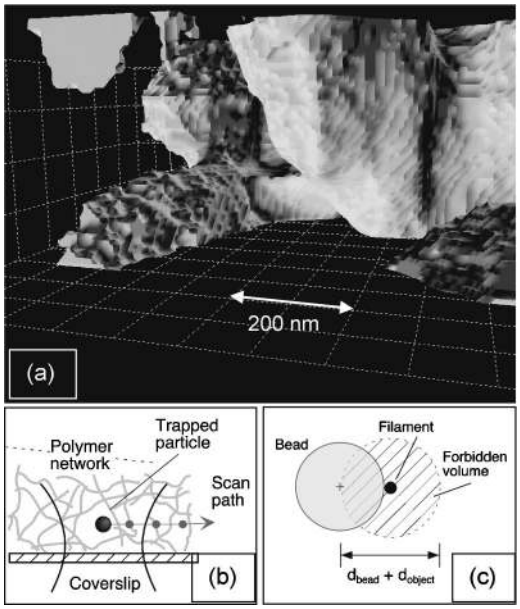

FIG. 12. Thermal noise imaging: (a) The structure represents the volume not accessible to the center of the fluctuating bead. The surfaces shown correspond to frequency isosurfaces from three-dimensional position histograms of a 216 nm bead trapped by the PFM in an Agar network. (b) The position of the trap was laterally scanned inside the network with a step width of 80 nm. (c) Mechanical amplification effect. A mechanically stiff filamentous object with a diameter d_{object} will appear in a thermal noise scan as a cylinder with a minimal diameter of $d_{\mathrm{min}} = d_{\mathrm{bead}} + d_{\mathrm{object}}$.

The detector can be calibrated by assuming that the signal $S_i'(\mathbf{r}) \approx g_i' x_i$ $(i = x,y,z)$ at position $\mathbf{r}$ is proportional to the particle displacement along x_i by a calibration factor g_i'. This is only approximately true, as illustrated by the non-Euclidic grid in Fig. 5(g). It is known from Eq. (6) that the width of the actual position distribution $p_B(x_i)$ must be $\sigma_i = (k_B T/k_i)^{1/2}$. This is also expressed by the equipartition theorem, which distributes $1/2 k_B T = 1/2 k_i \sigma_i^2$ to each degree of freedom. The assumption that the widths σ_i and σ_i' are proportional to each other by the factor $g_i' = \sigma_i'/\sigma_i$ results in the relation between the position signal and position:

$$S_i'(\mathbf{r}) = g_i' x_i = \sigma_i'/(k_B T/k_i)^{1/2} x_i. \tag{14}$$

If necessary $S_i(\mathbf{r})$ can be obtained by $S_i'(\mathbf{r})/S_0'$ according to Eq. (4). The detector sensitivity $g_i' = \sigma_i'/(k_B T/k_i)^{1/2}$ depends first on the width σ_i', which is determined by the physical light scattering at the particle and the subsequent amplification of the detector signals S_i'. Second, it depends on the trap stiffness k_i and with that on the strength of focusing.

VIII. THERMAL NOISE IMAGING

The photonic force microscope can be used as an imaging device by scanning the optical trap and thus the probe across a sample surface. As illustrated in Fig. 2(b) an object can be placed in the trapping volume to reveal detailed in-

formation of the interaction of the trapped particle and the object. This concept is illustrated in Fig. 9 where the bead movement was restricted by the flat surface of a coverslip. Since a weakly trapped probe applies only thermal forces to a sample, it is even possible to probe soft, biological material without causing damage. The technique of scanning structures with a thermally fluctuating bead is called thermal noise imaging.[23] It is an extension of scanning probe microscopy to three dimensions. In this study a nanosphere with a diameter of 216 nm was optically trapped within a polymer network, sketched in Fig. 12(b). At each position of the optical trap the center position of the bead was recorded for 0.8 s at a data acquisition rate of 100 kHz and histograms were calculated with a bin width of 8 nm. The bead could potentially explore a volume of about ± 60 nm in the lateral direction and about ± 150 nm in the axial direction at each position of the optical trap. By moving the trap through the network and subsequent superposition of the histograms it is possible to probe larger volumes. In the example shown in Fig. 12(a) a total volume of $(1.0\times 1.0\times 0.4)\ \mu m^3$ was imaged in three dimensions. The surface represents those voxels where the center of the fluctuating bead entered five times, and encloses the volume not accessible to the bead center. By considering the radius of the bead [i.e., the mechanical amplification effect, Fig. 12(c)], the filament structure appears thinner. The fine structures perceivable on the surface are an effect of the small number of events.

IX. DISCUSSION

A novel optical trapping and imaging system that exploits thermal noise, called a photonic force microscope, has been designed, built, and tested. It excels in mechanical stability, position detector sensitivity, and trapping efficiency. This study presents and characterizes its most important components. We also showed which features of the trapping and tracking system are already at their physical limit, and which other parts depend on currently available technology. We measured and explained the system's inherent background noise, nonlinearities of the 3D particle detection system, and physical asymmetry effects of optical traps.

Laser powers between 50 and 100 mW have often been used for trapping applications in cell biology. Although in the near-infrared (NIR) regime, this causes severe cell damage after only a few seconds.[58–60] It is therefore a challenge to achieve stable trapping with laser powers below 10 mW or, in other words, to generate optical traps with a maximum trapping force per laser power to minimize photodamage. We have achieved an excellent trapping efficiency (or trap stiffness per laser power $q=k/P$, respectively) by well centered, two-fold overillumination of the BFP of the trapping lens, which is a NIR water immersion objective lens (NA=1.2). For a 0.53 μm latex bead the efficiency k/P is about 1.8 pN/(μm mW) in the lateral direction and about 0.35 pN/(μm mW) in the axial direction. For a 0.22 μm latex bead k/P is about 0.28 pN/(μm mW) laterally and about 0.04 pN/(μm mW) axially.

It was also shown that stable trapping is possible for a 93 nm latex bead at $P=46$ mW leading to a very soft axial spring constant of $k_z=0.23$ pN/μm. Such a small trapping stiffness is useful when the bead needs to be held in the focus for position detection while thermal forces probe a molecule tethered to the bead. On the other stiffness extreme, at laser power of 80 mW in the focal plane, a lateral stiffness of $k_y=230$ pN/μm could be measured for a 1 μm latex bead, which is three orders of magnitude larger than k_z of the 93 nm bead. This strong trap stiffness offers the opportunity for several single molecule experiments with pulling forces of up to 100 pN at a moderate laser power. We applied a laser power of not more than $P=0.6$ mW to achieve stable trapping in three dimensions for a 0.53 μm latex bead, to our knowledge the smallest trapping laser power ever reported. The outstanding trapping efficiency favors experiments in live cell biology since it minimizes photodamage. Due to the large axial trap extension, large positive particle displacements are detected in the nonlinear range of the detector, which lead to a buckling of the axial position histogram and the trapping potential. This effect, enhanced by the additional phase shift through the particle, is discussed in Ref. 40 and can be compensated as explained in Ref. 46.

Detector nonlinearities that arise also have to be taken into account when the volume accessible to the fluctuating probe is shifted about 100–200 nm in the axial direction and 50–100 nm in the lateral direction. This may occur for a reduced trapping volume due to penetration of an object, which can be a flat interface in the simplest case. This leads to a deformation of the position histogram in addition to the change by the penetrating object. However, by carefully steering the trap in steps defined by the trapping volume and by carefully analyzing the position histograms, it is possible to image the surfaces of those volumes that are not accessible to the probe (thermal noise imaging).

Effects such as refractive index mismatch (spherical aberrations),[40,61] inhomogeneous or oblique illumination of the back focal plane, phase distortions, lens type (the planarity of the lens), or electric field polarization have a strong influence on the stiffness of an optical trap. We have not found even one experimental study where at least the majority of these effects have been considered and reported. It is therefore difficult to draw conclusions when coincidence with theoretical studies is reported that neglect these effects too. We recently investigated theoretically trapping forces and stiffnesses, where effects such as spherical aberrations for different distances to the coverslip or illumination of the BFP strongly influenced the trapping efficiency.[40] That study compares our simulation results to the measured results from various trapping situations described in experiments performed during the several last years by numerous authors. As expected, the coincidence varied. On the one hand, some critics alleged that our theory was not complete enough; on the other hand, some of the specified experimental alignments and measurements were possibly not sufficiently well described. However, by taking all relevant parameters into account, we measured a linear dependence between the trap stiffnesses in x, y, and z and the laser power in the focal plane. Up to a power of $P=60$ mW the coincidence between theory and experiment was excellent for the latex bead with a nominal diameter of 535 nm and still very good for the

latex bead with a nominal diameter of 216 nm. For both beads the stiffnesses in x, y, and z are all different and this illustrates the predicted strong influence of polarization. For the smaller bead the discrepancy between theory and experiment is 15%–20% in lateral direction, which is still an unequaled small difference. It remains unclear why the trap stiffnesses do not increase linearly for laser powers $P > 60\,\mathrm{mW}$, or, in other words, why the autocorrelation time $\tau_i = \gamma / k_i$ is larger than expected.

In summary, we presented a novel trapping and tracking setup exploiting thermal fluctuations of the probe. This system sets new milestones in stability, sensitivity, and efficiency and comes very close to the physical limit.

ACKNOWLEDGMENTS

The authors thank Dr. Jim Swoger for carefully reading the manuscript and Bo-Jui Chang for helpful comments. Special thanks to Leo Burger, Helmut Schaar, and Henry Werner at EMBL's mechanical workshop as well as to Georg Ritter and Alfons Riedinger at EMBL's electronic workshop.

[1] G. Binnig, H. Rohrer, C. Gerber, and E. Weible, Phys. Rev. Lett. **49**, 57 (1982).
[2] G. Binnig, C. F. Quate, and C. Gerber, Phys. Rev. Lett. **56**, 930 (1986).
[3] A. Ashkin, Opt. Lett. **9**, 454 (1984).
[4] A. Ashkin, J. M. Dziedzic, J. E. Bjorkholm, and S. Chu, Opt. Lett. **11**, 288 (1986).
[5] A. Ashkin and J. M. Dziedzic, Science **235**, 1517 (1987).
[6] A. Ashkin, J. M. Dziedzic, and T. Yamane, Nature (London) **330**, 769 (1987).
[7] S. M. Block, D. F. Blair, and H. C. Berg, Nature (London) **338**, 514 (1989).
[8] S. Seeger, S. Monajembashi, K. J. Hutter, G. Futterman, J. Wolfrum, and K. O. Greulich, Cytometry **12**, 497 (1991).
[9] R. W. Steubing, S. Cheng, W. H. Wright, Y. Numajiri, and M. W. Berns, Cytometry **12**, 505 (1991).
[10] Y. Tadir, W. H. Wright, O. Vafa, T. Ord, R. H. Asch, and M. W. Berns, Fertil. Steril. **52**, 870 (1989).
[11] K. Schutze, A. Clement Sengewald, and A. Ashkin, Fertil. Steril. **61**, 783 (1994).
[12] S. M. Block, L. S. Goldstein, and B. J. Schnapp, Nature (London) **348**, 348 (1990).
[13] A. Ashkin, K. Schutze, J. M. Dziedzic, U. Euteneuer, and M. Schliwa, Nature (London) **348**, 346 (1990).
[14] S. C. Kuo and M. P. Sheetz, Science **260**, 232 (1993).
[15] K. Svoboda, C. F. Schmidt, B. J. Schnapp, and S. M. Block, Nature (London) **365**, 721 (1993).
[16] T. T. Perkins, D. E. Smith, and S. Chu, Science **264**, 819 (1994).
[17] S. B. Smith, Y. Cui, and C. Bustamante, Science **271**, 795 (1996).
[18] M. D. Wang, H. Yin, R. Landick, J. Gelles, and S. M. Block, Biophys. J. **72**, 1335 (1997).
[19] K. Visscher, M. J. Schnitzer, and S. M. Block, Nature (London) **400**, 184 (1999).
[20] R. M. Simmons, J. T. Finer, S. Chu, and J. A. Spudich, Biophys. J. **70**, 1813 (1996).
[21] E.-L. Florin, J. K. H. Hörber, and E. H. K. Stelzer, Appl. Phys. Lett. **69**, 446 (1996).
[22] E.-L. Florin, A. Pralle, J. K. H. Hörber, and E. H. K. Stelzer, J. Struct. Biol. **119**, 202 (1997).
[23] C. Tischer, S. Altmann, S. Fisinger, J. K. H. Hörber, E. H. K. Stelzer, and E.-L. Florin, Appl. Phys. Lett. **79**, 3878 (2001).
[24] A. Pralle, E.-L. Florin, E. H. K. Stelzer, and J. K. H. Hörber, Appl. Phys. A: Mater. Sci. Process. **A66**, S71 (1998).
[25] A. Pralle, P. Keller, E.-L. Florin, K. Simons, and J. K. H. H. Hörber, J. Cell Biol. **148**, 997 (2000).
[26] S. Jeney, E.-L. Florin, and J. K. H. Hörber, in *Kinesin Protocols*, edited by I. Vernos (Humana, Totowa, NJ, 2000), Vol. 194, pp. 91–107.
[27] A. Rohrbach, E. L. Florin, and E. H. K. Stelzer, Proc. SPIE **4431**, 75 (2001).
[28] L. Malmqvist and H. M. Hertz, Opt. Commun. **94**, 19 (1992).
[29] L. P. Ghislain and W. W. Webb, Opt. Lett. **18**, 1678 (1993).
[30] S. Kawata, Y. Inouye, and T. Sugiura, Jpn. J. Appl. Phys., Part 2 **33**, L1725 (1994).
[31] T. Sugiura, T. Okada, Y. Inouye, O. Nakamura, and S. Kawata, Opt. Lett. **22**, 1663 (1997).
[32] M. E. J. Friese, A. G. Truscott, H. Rubinsztein-Dunlop, and N. R. Heckenberg, Appl. Opt. **38**, 6597 (1999).
[33] K. Svoboda, C. F. Schmidt, B. J. Schnapp, and S. M. Block, Nature (London) **365**, 721 (1993).
[34] L. Ghislain, N. Switz, and W. Webb, Rev. Sci. Instrum. **65**, 2762 (1994).
[35] M. E. Friese, H. Rubinsztein-Dunlop, N. R. Heckenberg, and E. W. Dearden, Appl. Opt. **35**, 7112 (1996).
[36] K. Sasaki, M. Tsukima, and H. Masuhara, Appl. Phys. Lett. **71**, 37 (1997).
[37] A. Pralle, M. Prummer, E.-L. Florin, E. H. K. Stelzer, and J. K. H. Hörber, Microsc. Res. Tech. **44**, 378 (1999).
[38] A. R. Clapp and R. B. Dickinson, Langmuir **17**, 2182 (2001).
[39] M. J. Lang, C. L. Asbury, J. W. Shaevitz, and S. M. Block, Biophys. J. **83**, 491 (2002).
[40] A. Rohrbach and E. H. K. Stelzer, Appl. Opt. **41**, 2494 (2002).
[41] F. Reif, *Fundamentals of Statistical and Thermal Physics* (McGraw–Hill, Auckland, NZ, 1985), pp. 560–565.
[42] A. Rohrbach and E. H. K. Stelzer, J. Appl. Phys. **91**, 5474 (2002b).
[43] A. Rohrbach, H. Kress, and E. H. K. Stelzer, Opt. Lett. **28**, 411 (2003).
[44] M. Born and E. Wolf, *Principles of Optics*, 7th ed. (Cambridge University Press, New York, 1999).
[45] B. E. A. Saleh and M. C. Teich, *Fundamentals of Photonics* (Wiley, New York, 1991).
[46] C. Tischer, A. Pralle, and E.-L. Florin, Microsc. Microanal. **10**, 1 (2004).
[47] A. Rohrbach and E. H. K. Stelzer, J. Opt. Soc. Am. A **18**, 839 (2001).
[48] H. C. van de Hulst, *Light Scattering by Small Particles* (Dover, Leiden, Germany, 1957).
[49] R. Gussgard, T. Lindmo, and I. Brevik, J. Opt. Soc. Am. B **9**, 1922 (1992).
[50] T. Wohland, A. Rosin, and E. H. K. Stelzer, Optik (Stuttgart) **102**, 181 (1996).
[51] J. P. Barton, D. R. Alexander, and S. A. Schaub, J. Appl. Phys. **66**, 4594 (1989).
[52] F. Ren, G. Gréhan, and G. Gouesbet, Opt. Commun. **108**, 343 (1994).
[53] K. Visscher and G. J. Brakenhoff, Optik (Stuttgart) **89**, 174 (1992).
[54] Y. Harada and T. Asakura, Opt. Commun. **124**, 529 (1996).
[55] E.-L. Florin, A. Pralle, E. H. K. Stelzer, and J. K. H. Hörber, Appl. Phys. A: Mater. Sci. Process. **A66**, S75 (1998).
[56] F. Gittes and C. F. Schmidt, Methods Cell Biol. **55**, 129 (1998).
[57] The mass of a 1 μm diam latex bead (density 1060 kg/m^3) is about 4.2×10^{-16} kg (kg=N s^2/m). The viscous drag of this sphere is $\gamma = 9.5 \times 10^{-9}$ N s/m in water at $T = 23\,^\circ$C ($\eta = 9.35\ \mu$Pa s). Therefore the ratio $m/g = 4.4 \times 10^{-8}$ s is still much smaller than the shortest measurable change in signal of $\tau = 2 \times 10^{-6}$ s.
[58] K. König, H. Liang, M. W. Berns, and B. J. Tromberg, Opt. Lett. **21**, 1090 (1996).
[59] K. C. Neuman, E. H. Chadd, G. F. Liou, K. Bergman, and S. M. Block, Biophys. J. **77**, 2856 (1999).
[60] P. Celliers and C. J. Chu, Appl. Opt. **39**, 3396 (2000).
[61] P. C. Ke and M. Gu, J. Mod. Opt. **45**, 2159 (1998).